A novel test rig to investigate under-platform damper dynamics

A novel test rig to investigate under-platform damper dynamics

Daniele Botto[a,*], Muhammad Umer[a]

[a] *Politecnico di Torino, Department of Mechanical and Aerospace Engineering, corso Duca degli Abruzzi, 24 - 10129 Torino, Italy*

Abstract

In the field of turbomachinery, vibration amplitude is often reduced by dissipating the kinetic energy of the blades with devices that utilize dry friction. Under-platform dampers, for example, are often placed in the underside of two consecutive turbine blades. Dampers are kept in contact with the under-platform of the respective blades by means of the centrifugal force. If the damper is well designed, vibration of blades instigate a relative motion between the under-platform and the damper. A friction force, that is a non-conservative force, arises in the contact and partly dissipates the vibration energy. Several contact models are available in the literature to simulate the contact between the damper and the under-platform. However, the actual dynamics of the blade-damper interaction have not fully understood yet. Several test rigs have been previously developed to experimentally investigate the performance of under-platform dampers. The majority of these experimental setups aim to evaluate the overall damper efficiency in terms

*Corresponding author

Email addresses: daniele.botto@polito.it (Daniele Botto), muhammad.umer@polito.it (Muhammad Umer)

URL: www.dimeas.polito.it (Daniele Botto)

of reduction in response amplitude of the blade for a given exciting force that simulates the aerodynamic loads. Unfortunately, the experimental data acquired on the blade dynamics do not provide enough information to understand the damper dynamics. Therefore, the uncertainty on the damper behavior remains a big issue.

In this work, a novel experimental test rig has been developed to extensively investigate the damper dynamic behavior. A single replaceable blade is clamped in the rig with a specific clamping device. With this device the blade root is pressed against a groove machined in the test rig. The pushing force is controllable and measurable, to better simulate the actual centrifugal load acting on the blade. Two dampers, one on each side of the blade, are in contact with the blade under-platforms and with platforms on force measuring supports. These supports have been specifically designed to measure the contact forces on the damper. The contact forces on the blade are computed by post processing the measured forces and assuming the static equilibrium of the damper. The damper kinematics is rebuilt by using the relative displacement, measured with a differential laser, between the damper and the blade under-platform.

This article describes the main concepts behind this new approach and explains the design and working of this novel test rig. Moreover, the influence of the damper contact forces on the dynamic behavior of the blade is discussed in the result section.

Keywords:

Turbine blade vibrations Nonlinear dynamics Friction damping
Under-platform damper Test rig Contact force measurement

---

1. Introduction

1.1. Background and motivation

Gas and steam turbines is a widespread technology in power and thrust generation, commonly used in power plants, aircrafts, helicopters, ships, etc. Turbine blades undergo variable aerodynamic loads that are a potential source of detrimental vibrations. If the frequency of the cyclic aerodynamic loads is close to a blade/disk resonance the amplitude of the vibration increases and the blade could experience fatigue damage, that in the worst case leads to its failure. To reduce the vibration amplitude to a safe limit external damping is added to the blade. Devices such as Under-Platform Dampers (UPD), tip or part-span shrouds and damper rings are commonly used to reduce the vibration amplitude in turbine blades. These devices dissipate the friction energy of two contact surfaces that move relative to each other. The working principle of UPDs is described with the help of Fig. 1, that shows a common configuration in which one damper is inserted between two consecutive blades. The centrifugal force F_C pushes the damper against the blades so that the upside of the damper makes a contact with the left and right blade under-platforms. In static conditions, i.e. neglecting the blade dynamics, the normal contact forces are constant and depend on the nature of the contact between the damper and the under-platform. When the blades vibrate, the damper dynamics come into play and the normal contact forces are no longer constant. Moreover, if the damper and the under-platforms undergo a relative motion, a tangential force develops on the contact surfaces. The tangential force T increases with the relative displacement δ up to its maximum value, namely the normal contact force N times the friction

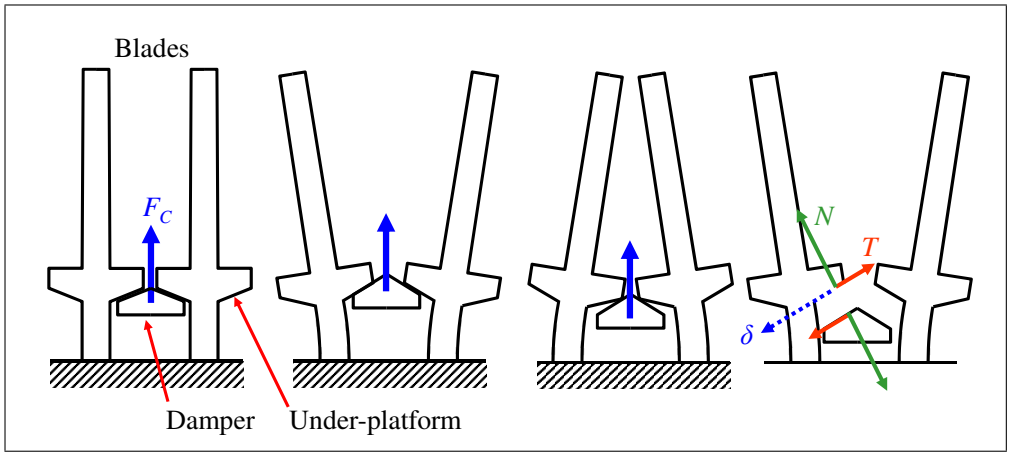

Figure 1: sketch of an under-platform damper/blade configuration.

coefficient $T = \mu N$. Characteristics of the frictional contacts are commonly described by hysteresis loops, which present the change in tangential force with respect to the relative displacement [1]. The enclosed area of the hysteresis loop is to the energy dissipated in the contact, which in turn is related to the damping property of the contact. The slope of the hysteresis loop at the onset of the relative motion is denoted as contact stiffness. Both the dissipated energy and the contact stiffness affect the dynamic behavior of the blade assembly.

Several test rigs were previously developed to experimentally investigate the effect of the under-platform damper on the blade dynamics. In [2] an experimental apparatus made with a single blade/single damper was developed to measure the damper performance in terms of vibration stress reduction. The experimental results were used to assess the capability of a new contact model [3]. Nowadays, a typical test rig architecture is composed by one damper placed between two blades excited with a shaker [4, 5, 6, 7, 8]. In [9] and

later in [10] also the damper rotation was measured to better understand the damper kinematics. A modified architecture was used in [11, 12] in which two dampers were in contact with the different platforms of the same test blade. The other side of the damper was in contact with a more rigid structure called dummy blade. Moreover, the blade was excited by a pulsating air jet. In all these experimental setups the centrifugal force acting on the damper was simulated by a static force applied by dead weights attached to the damper through a wires and pulleys arrangement or solid strips. In a more complex test rig [13] a 24 blades assembly was excited with a rotating force to investigate the damper behavior at different nodal diameters. In this rig, dampers were loaded with dead weights as well. Dampers are loaded in a more realistic way when tests are performed with a rotating disks. In this regard, in [14] an experimental and numerical study was carried out on a thin-walled damper in a rotating disk with blades excited with piezoelectric actuators. The test rig described in [15, 16] was used to measure the effect of wedge shaped dampers on the dynamic response of a simple bladed disk. In this test rig, a non-contact magnetic excitation was applied along with a non-contact measuring system. The previously cited experimental setups, which are not exhaustive of all the test rigs that can be find in the literature, aimed to study the overall effect of the damper on the blade dynamics in terms of vibration amplitude reduction and resonant frequency shift. This black-box like approach is functional to evaluate the capability of the damper to reduce displacements at resonance, but it does not provide a better comprehension of the damper behavior. These test rigs are not capable of analyzing the dynamics of the damper in depth, nor its kinematics in terms

of damper/under-platform relative displacement. On the other side several test rigs [17, 18, 19, 20, 21, 22, 23] were developed to measure the contact parameters, namely friction coefficient and contact stiffness, in controlled laboratory conditions. The need for measuring the contact parameters on a damper in working conditions led to AERMEC's first Damper Test Rig. This rig was built in 2008 [24] and was a first step towards a deep investigation of dampers kinematics. In this rig, piezoelectric actuators, feedback controlled, move the under-platforms with a given rule. Since then, the test rig has been used to investigate the behavior of several dampers in terms of kinematics and force transmission characteristics [25, 26]. A numerical model of the damper/test-rig system was first presented in [27], together with the first version of the contact parameters estimation procedure, subsequently improved in [28].

1.2. Objectives

The overall objective of this work is to develop an experimental setup to better investigate and understand the dynamic behavior of the damper when it is coupled with the blade. To achieve this goal a novel test rig was designed with the purpose to measure both the forces on the contact and the damper kinematics. It was underlined in [29, 30] that the static forces on the damper are of paramount importance for the overall damper/blade dynamics. With respect to this reference, the developed test rig is also required to measure and record the static contact forces on the damper. The first part of this paper describes the design specifications and experimental competencies of this novel test rig. The second part discusses the blade dynamic in the light of the observed damper behavior and the frequency response of the blade is

correlated with the contact forces measured on the dampers.

2. Test rig design

The test rig has been developed to fulfill the following specifications:

1. an assembly of a single blade and two dampers must be tested. The dampers are in contact with the under-platform of the blade on one side and with a ground platform on the other side.
2. Contact pads on the ground platform can be manufactured with different materials and contact angles to investigate several contact geometries of dampers and blades. The contact pads must be replaceable, providing cost advantage to replacement of the whole ground platform.
3. The rig should allow testing different turbine blades with minor adjustment of the apparatus, provided the maximum blade size is not exceeded.
4. The designed test bench must be capable of measuring the damper contact forces on the ground platforms.
5. A regulated and measurable clamping force is required to apply a force on the blade which simulates the effect of the actual centrifugal load while turbine runs.
6. The test rig must allow measuring the relative displacement between the contact surfaces.

The test rig, whose full sketch is depicted in Fig. 2, is composed of three main sub-assemblies, namely a central block and two lateral blocks. The central block is made of two symmetric parts, (1A) and (1B), fixed to a base

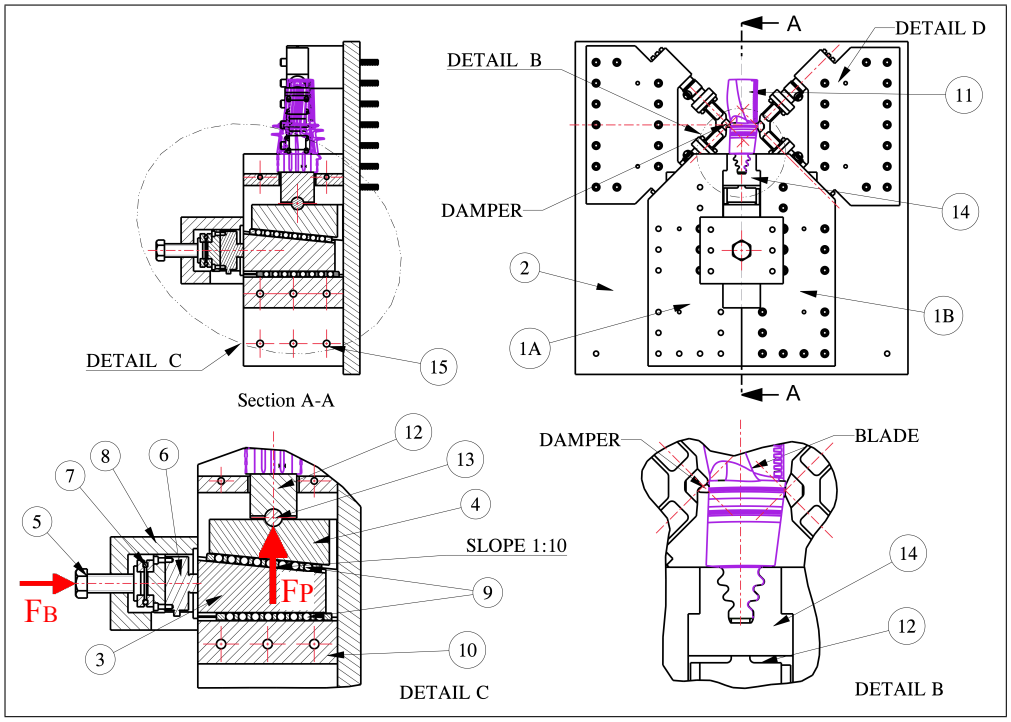

Figure 2: test rig overview.

plate (2) with 32 vertical bolts. These two symmetric parts house the blade and a clamping mechanism to apply a static force simulating the centrifugal load on the blade. The clamping mechanism is made of two wedge blocks, the lower wedge (3) and the upper wedge (4), with a slope of 1:10. These wedges convert a force F_B applied perpendicular to the longitudinal axis of the blade into a pushing force F_P acting along the blade longitudinal axis. The force F_B is developed by tightening the main Bolt (5) on the bottom wedge (3). Due to the given slope between the two wedges, the nominal force amplification factor A_n between the bolt force F_B and the pushing force F_P is 10. A load cell based on strain gauge (6) is placed between the main bolt (5) and the lower wedge block (3). This load cell measures the bolt force F_B. A thrust ball bearing (7) is placed between the main bolt and the load cell to allow their relative rotation. The subassembly composed of the main bolt, the thrust ball bearing and the load cell is enclosed in a casing (8). The casing is tightened with six screws to the central block. Two rails of linear flat roller bearings (9) are introduced between the sliding surfaces to minimize the friction losses. The first rail is inserted between the lower wedge (3) and the bottom fixed block (10). The second rail is located between lower and upper wedge. However, it is not possible to remove all friction losses in the clamp mechanism and rolling friction still cause a small loss in the clamping force. The clamping force F_P acting on the blade root and the actual amplification factor A_{act} can be calculated with the following formulas

$$F_{P,act} = \frac{cos\alpha - 2\,\mu\, sin\alpha - \mu^2\, cos\alpha}{sin\alpha + 2\,\mu\, cos\alpha - \mu^2\, sin\alpha} F_B, \quad (1)$$

$$A_{act} = \frac{F_{P,act}}{F_{B,act}}, \quad (2)$$

whereas μ and α are the rolling friction coefficient of the linear bearings and the wedges' slope respectively. The clamp efficiency $\eta_c = A_{act}/A_n$ is defined as the ratio between the actual and the nominal amplification factor. Since the friction coefficient of the linear bearings ranges between $\mu = 0.001 \div 0.0015$, as reported in [31], the overall efficiency of the clamping mechanism ranges between $\eta_c \approx 0.97 \div 0.98$. The pushing force F_P is transmitted to the blade (11) through the pushing block (12). An aligning pin (13) allows small rotation between the upper wedge and the pushing block. The aligning pin allows to apply a uniform pressure at the blade root even with small misalignment between the blade and the upper wedge. To avoid excessively high contact pressure, the self-aligning pin and its counterparts were designed with conforming contact surfaces. The pressure distribution on conforming contact surface was deduced by tables and graphs given in [32]. The blade is inserted in an adapter (14) in which a bucket groove was machined to match the blade root geometry. The blade adapter is pushed against the shoulders on the central block. As the blade adapter is replaceable, blades with different root can be tested by simply changing the adapter according to the new geometry. Eight long stud bolts are inserted across the two parts of the central block, through holes (15), to complete the assembly. These stud bolts work in addition to the vertical bolts and increase the stiffness of the structure.

2.1. Damper Contact Force Measurement System

Measuring the contact forces acting on the damper is a significant feature of this novel test rig. Two force-measuring systems, one on each side of the blade, are available to measure the contact forces on both dampers. The

measuring devices are shown in Fig. 3, with N and T being the normal and tangential components of the contact force respectively. Each force measuring system is composed of an L-shaped structure with two limbs (16A and 16B) named as L-Separator (17), L-Sep in short, two piezoelectric load cells – $LC_{11,13}$ and $LC_{12,14}$ – and a lateral block (18). The two limbs of the L-Sep are orthogonal to each other and each limb is composed of two thin parallel strips as shown in Fig. 3. The axes of both limbs intersect each other at the point of the nominal contact between the damper and the pad. The complete design strategy and working principle of the L-Sep are described in Sec. 2.2. The two load cells LC are fixed at the free end of both limbs with the help of two connecting blocks (19A and 19B). Each load cell is coaxial with the limb, coaxiality being ensured by centering rings. The load cells are fastened to the lateral block (18). The lateral blocks are fixed to the optical table with 14 vertical bolts passing through the base plate. Two aligning-pin holes (20A and 20B) on the lateral block (18) ensure the proper location of the force measuring system with respect to the damper position.

2.2. L-Separator design criteria

The L-Separator is purposely designed to separate the contact force into two components acting along the limb axes. With the proposed shape and geometry the load cells experience only axial force. The transverse force is negligible, and the crosstalk effect is prevented. This goal was achieved by designing the contact point at the intersection of the limbs axes and each limb with a substantially high ratio between the longitudinal and the transverse stiffness k_l/k_t. Indeed, with reference to Fig. 4, if the L-Sep is loaded with a force along the axis of one limb the reaction force on the load cells are in

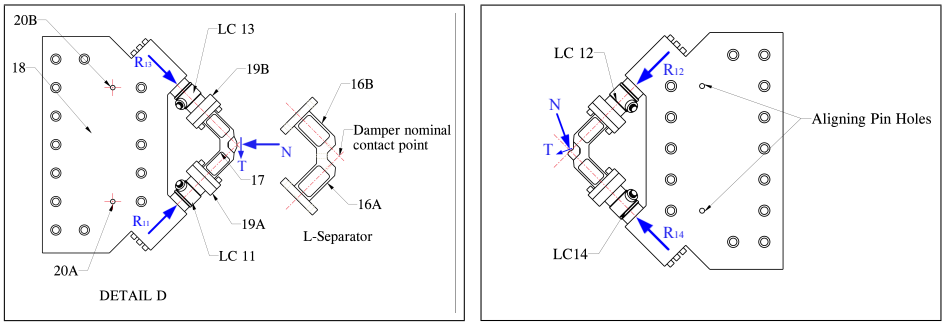

(a) Contact force Measuring system on the odd side

(b) Contact force Measuring system on the even side

Figure 3: Geometry and contact forces on odd and even sides.

the same ratio as the stiffnesses,

$$\frac{R_{Y1}}{R_{Y2}} = \frac{k_l}{k_t}. \tag{3}$$

A simple model of the L-Sep, made of beams and lumped masses, was used in the preliminary design to compute the degree of separation, namely the ratio between the axial reaction on the load cell and the applied force along the axis of the respective limb, R/F. The graph in Fig. 5 shows the degree of separation plotted against the aspect ratio ratio L/b with different strip thicknesses t, where L and b are length and breadth of the limb strip respectively. According to this analysis, at the design point $L/b = 1$ and $t = 1.5\,\text{mm}$, the degree of separation is 99.4 %. The results of the preliminary design were confirmed by a full finite element (FE) analysis of the L-Sep at the selected dimensional parameters. In this calculation, the load cell stiffness was also included. Figure 6 shows the L-Sep FE model loaded with a force F along the axis of one limb. The reaction force R on the load cell is 0.995 F, namely with a degree of separation of 99.5 %, a result that is in good

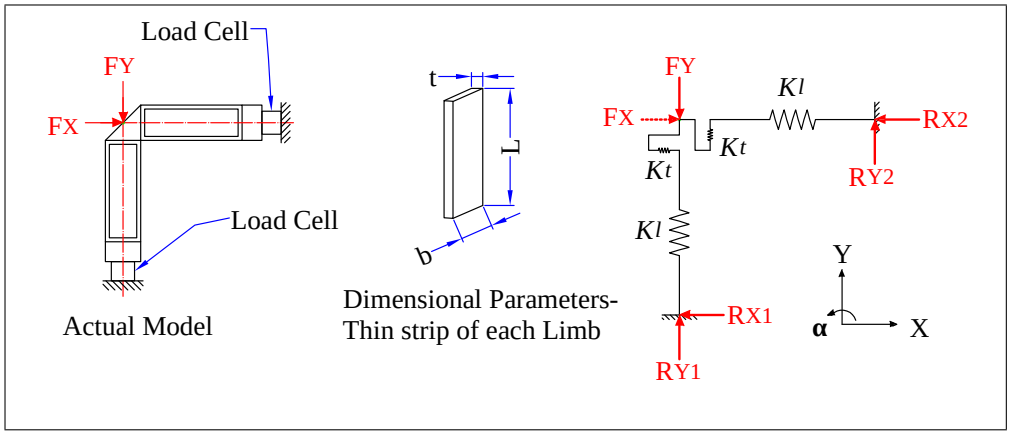

Figure 4: Basic model of L-Separator

agreement with the simplified model depicted in Fig. 4. These results were used in the post-processing of measured data to correct the load cells signals and evaluate the actual contact forces.

3. Contact forces calculation

Figures 7 and 8 show the angles that define the contact geometry and the forces on the "*odd*" and "*even*" side respectively. The even side comprises the load cells 12 and 14, while load cells 11 and 13 compose the odd side. The L-Sep is sketched in the drawing, while the blade is represented only through its contact points. In these figures the dampers are not in scale, they have been enlarged to show more clearly the contact area and forces.

The normal and tangential components of the contact force on the L-Sep, namely N_L and T_L, are directly inferred from the load cells signals. The components of the contact force on the blade, N_B and T_B, are derived by assuming the static equilibrium of the damper. The damper inertia forces

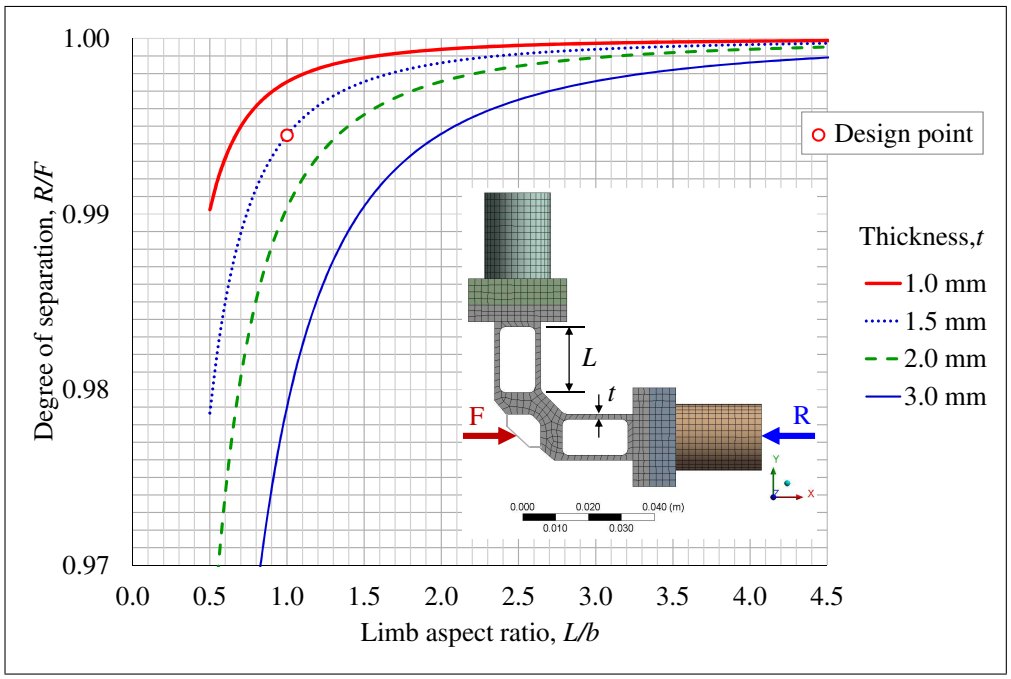

Figure 5: degree of separation with respect to the L-Separator dimensional parameters.

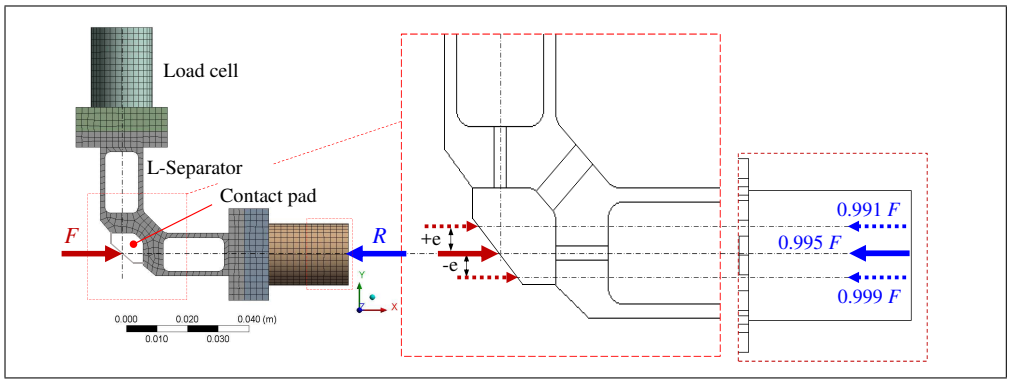

Figure 6: finite element model of L-Separator. Eccentricity e represents the location error due to manufacturing accuracy.

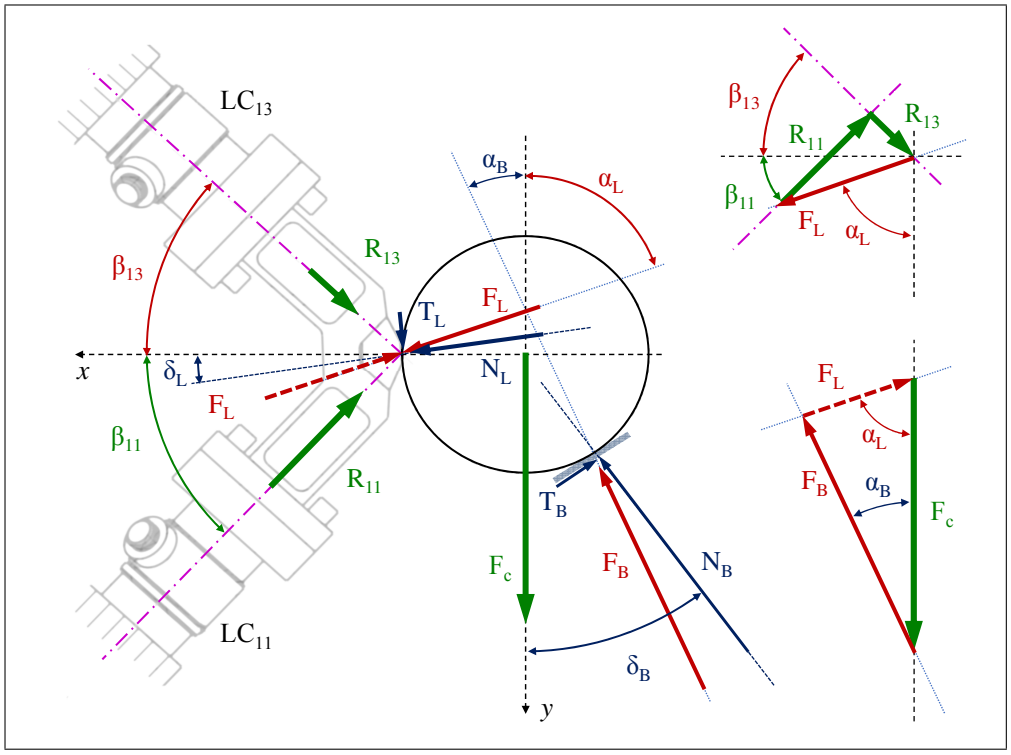

Figure 7: geometry and contact forces on the odd load cells LC_{11}/LC_{13} side. Positive forces and angles are depicted

were neglected because lower than 2 N in the frequency range of interest. All the force components are summarized in Table 1; notation and symbols are consistent with those used in Figs. 7 and 8.

4. Force measurement accuracy

The accuracy of the calculated contact forces, determined by processing the load cells measured signals, depends on many factors. The main sources of errors are listed below:

1. the accuracy of the acquisition system chain that comprises load cells,

Table 1: derived force components.

Odd side	Even side
On the L-Separator	
$F_L = \sqrt{R_{11}^2 + R_{13}^2}$	$F_L = \sqrt{R_{12}^2 + R_{14}^2}$
$sin\ \alpha_L = \frac{R_{11} cos\ \beta_{11} + R_{13} cos\ \beta_{13}}{F_L}$	$sin\ \alpha_L = \frac{R_{14} cos\ \beta_{14} - R_{12} cos\ \beta_{12}}{F_L}$
$cos\ \alpha_L = \frac{R_{11} sin\ \beta_{11} - R_{13} sin\ \beta_{13}}{F_L}$	$cos\ \alpha_L = \frac{R_{12} sin\ \beta_{12} + R_{14} sin\ \beta_{14}}{F_L}$
$N_L = F_L \cdot cos(\pi/2 - \alpha_L - \delta_L)$	$N_L = F_L \cdot cos(\delta_L - \alpha_L)$
$T_L = F_L \cdot sin(\pi/2 - \alpha_L - \delta_L)$	$T_L = F_L \cdot sin(\delta_L - \alpha_L)$
On the Blade	
$F_B = \sqrt{F_C^2 + F_L^2 - 2F_C F_L\ cos\ \alpha_L}$	$F_B = \sqrt{F_C^2 + F_L^2 - 2F_C F_L\ cos\ \alpha_L}$
$sin\ \alpha_B = sin\ \alpha_L \frac{F_L}{F_B}$	$sin\ \alpha_B = sin\ \alpha_L \frac{F_L}{F_B}$
$cos\ \alpha_B = \frac{F_C - F_L cos\ \alpha_L}{F_B}$	$cos\ \alpha_B = \frac{F_C - F_L cos\ \alpha_L}{F_B}$
$N_B = F_B \cdot cos(\delta_B - \alpha_B)$	$N_B = F_B \cdot cos(\pi/2 - \alpha_B - \delta_B)$
$T_B = F_B \cdot sin(\delta_B - \alpha_B)$	$T_B = F_B \cdot sin(\pi/2 - \alpha_B - \delta_B)$

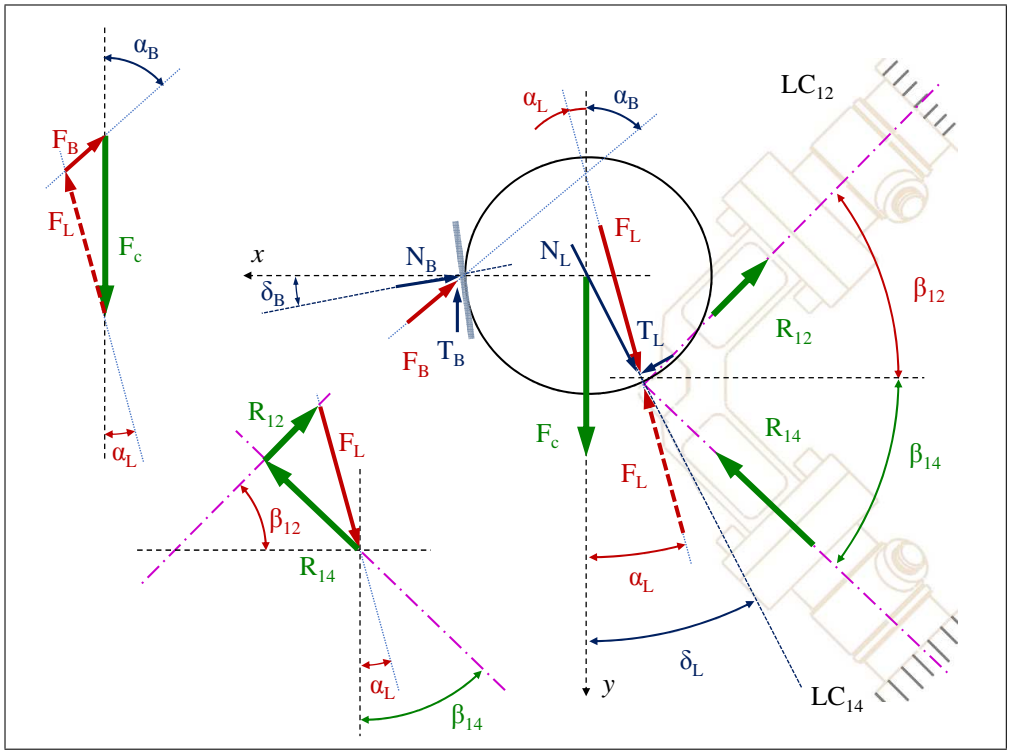

Figure 8: geometry and contact forces on the even load cells LC_{12}/LC_{14} side. Positive forces and angles are depicted

charge amplifiers and acquisition cards,

2. the dimensional and geometrical tolerances of the mechanical components
3. and the accuracy of the measured relative angle, δ_L and δ_B, between the static force F_c, simulating the centrifugal load applied to the damper, and the contact surface normal.

The force acting on the piezoelectric load cell generates a proportional electric charge at the output of the sensor which is converted by a charge amplifier into a voltage signal. The sensitivity of the load cells, namely charge per

unit force, is -9.6 pC/N. The load cell sensitivity joint with the resolution of the charge amplifier ± 0.1 pC gives a threshold of the measurable force of ± 10.4 mN. The error introduced by the charge amplifier is $< \pm 1\%$ of the full scale. A full scale of 200 N was used in the experimental campaign. The acquisition system is based on a 8 channel analog inputs card (simultaneous sampling at 1.25 MS/s/ch, 16-bit resolution). The accuracy of the card, in the voltage range ± 10V, is 3 mV thus giving an accuracy ± 0.06N on the measured forces corresponding to $< \pm 0.04\%$ of the full scale. Therefore, the estimated overall error due to the electronic instrumentation is $< \pm 1.05\%$

The relative position between the two platforms where the contact occurs, one on the L-Sep the other on the blade, is of paramount importance for a reliable force measurements. For this reason, the force measuring system and the blade clamping blocks were placed with location pins on the base plate. The overall error due to tolerances in the mechanical chain results in a mislocation of the contact point on the platform with respect to its nominal position. The nominal position of the contact point lies at the intersection of the load cells axes. Figure 6 shows the mislocation error in terms of eccentricity e. The tolerances chain gives a maximum value $e = \pm 1.5$ mm. Numerical analysis with a FE model were performed to calculate the reaction on the load cell when the contact force is located at its nominal position and at the maximum eccentricity. It was found that the mislocation introduces a deviation of the load cell reaction of $\pm 0.4\%$ with respect to the nominal value.

Each damper is in contact with the L-Sep. on one side and with the blade on the other side. The contact forces on the L-Sep. are directly measured

by the load cells. The normal and tangential force components on the blade are determined by imposing the static equilibrium of the damper. The force formulation of each contact is given in Table 1. The calculated contact forces are highly dependent on the orientation of the static force F_c on the damper with respect to the contact surfaces. These angles were deduced by post processing high-resolution images taken from the top of the test rig before starting the experimental campaign. The accuracy of the angles measured in this way was estimated as $\pm 1^\circ$. The error in the calculated contact forces due to the uncertainty in the angle measurement depends upon the specific geometry under observation and can be estimated with a sensitivity analysis. A numerical sensitivity analysis has been performed on the used particular geometry. The measured value of the angles $\delta_{L,B}$ and β_{1n} $(n = 1, \ldots, 4)$ have been varied by the angle measurement accuracy (1°). The corresponding variation in the contact forces N and T gives the sensitivity, namely force per unit angle. The variation of the contact forces has been determined with the equations in Table 1 using some sets of measured forces R_{1n} $(n = 1, \ldots, 4)$. Table 2 summarizes the sensitivity of the contact forces in the worst case. The accuracy of these forces has been evaluated by summing up the sensitivity of each force to the angle variation.

5. Experimental setup

Two different frameworks were used to measure the contact parameters and blade dynamics. One framework, framework-I, was used to measure the Frequency Response Function (FRF) of the blade with a stepped-sine excitation force. The feedback controlled force was applied near the blade

Table 2: sensitivity of contact forces to the specific damper/blade geometry

	Odd side, $i = 1$, $j = 3$				Even side, $i = 2$, $j = 4$			
Sensitivity, in N/°	N_L	T_L	N_B	T_B	N_L	T_L	N_B	T_B
$\frac{\partial}{\partial \delta_L}$	-0.6	1.1	0.0	0.0	-0.3	1.6	0.0	0.0
$\frac{\partial}{\partial \delta_B}$	0.0	0.0	-0.7	1.4	0.0	0.0	0.8	1.1
$\frac{\partial}{\partial \beta_{1i}}$	0.0	-0.1	-0.1	0.0	0.0	0.0	0.0	0.0
$\frac{\partial}{\partial \beta_{1j}}$	0.6	1.0	-0.8	-1.0	-0.3	-1.6	1.3	1.9
Accuracy, in N/°	1.2	2.2	1.6	2.4	0.6	3.2	2.1	3.0

root by a shaker/stinger arrangement. The excitation force was measured by a piezoelectric load cell LC_0 placed at the end of the stinger, while the response was measured by an accelerometer A_0, placed on the trailing side of the blade. This framework uses the Data Acquisition System-I (DAS-I) to develop the FRF of the blade from the measured force and acceleration. In framework-I, the signals were available in frequency domain only. The contact forces can be measured during FRF measurements, however the force control at each frequency step does not assure a reliable measurement.

In order to overcome this limitation, a second experimental framework-II, was introduced. In framework-II, the blade was excited with a sinusoidal force of single frequency. The excitation force amplitude was controlled by LC_0. The relative displacement between the blade and one damper was measured with a differential laser vibrometer (LDV). The LDV measures the out-of-plane velocity difference between two spots, one located on the blade, other on the damper. The spots were placed as close as possible to the contact point. The relative displacement was obtained with time integration of the

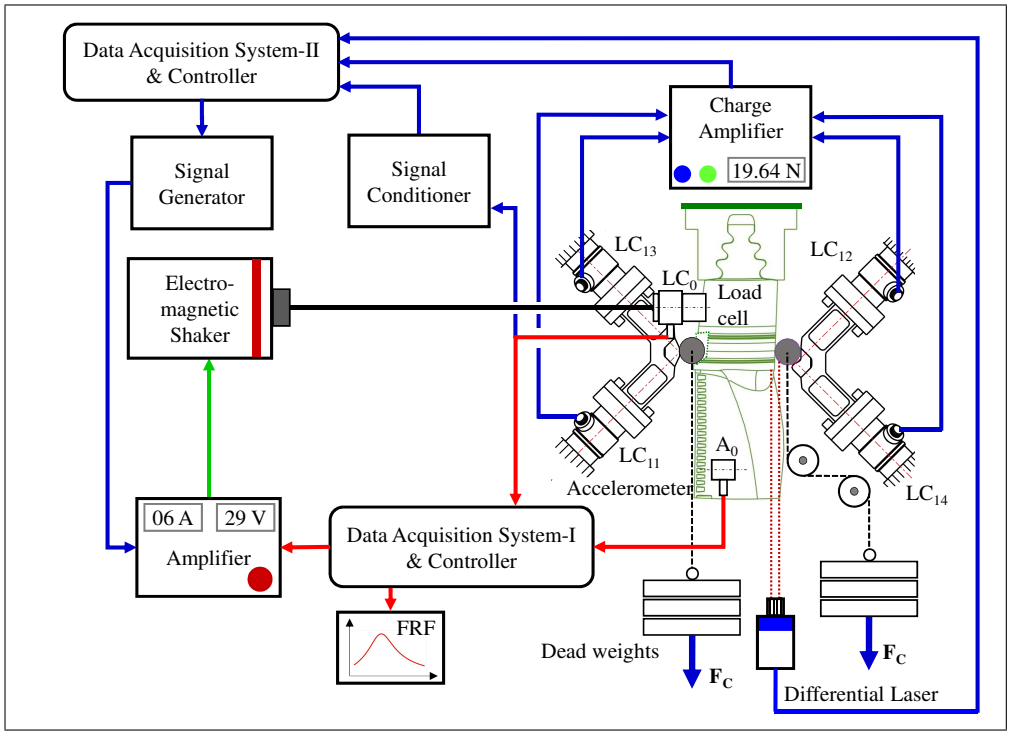

Figure 9: layout of the frameworks used to measure the frequency response function of the blade and the damper dynamics.

measured relative velocity. With this blade, only the damper on the even side was accessible by the laser beams. Data Acquisition System-II (DAS-II) collects both the signals from the laser head and the load cells LC_{11}, LC_{12}, LC_{13} and LC_{14}. Figure 9 shows the layout of both frameworks.

6. Experimental results and discussion

The experimental results presented in this section were obtained by using a real turbine blade and dampers. The blade and the dampers were made up of different materials: single crystal nickel based for the blade and isotropic

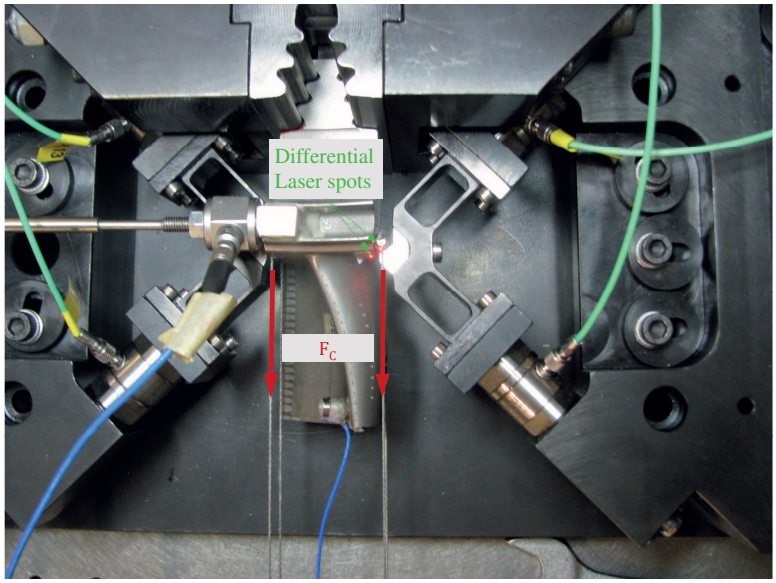

Figure 10: Detail of the blade/damper layout used in the tests.

cobalt alloy for the dampers. The contact angles are different for the two platform on the blade with $\delta_B = 1.7°$ and $\delta_B = 19.7°$ for the odd, Fig. 7, and even side, Fig. 8, respectively. Two cylindrical dampers, with diameter $D = 4.5$ mm, length L= 42 mm and mass m= 4.0 g, were used in these experiments. The centrifugal load on the dampers was simulated by a force applied in the form of dead weights using wires and pulleys arrangement, see Fig. 10. This force is referred to as *static force* F_c on the damper. Therefore, the mass of the damper does not affect the laboratory results.

The blade was clamped with a pushing force $F_P = 150$ kN that matches the actual working conditions. The first resonance of the clamped blade without dampers was measured around 1345 Hz, see Fig. 11. The results of two set of experiments are presented here. The first set was performed to

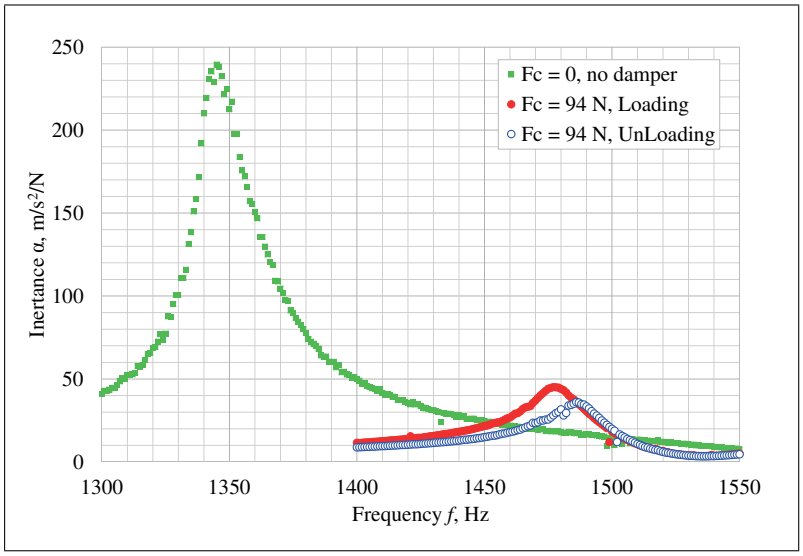

Figure 11: frequency response of the blade without dampers and with dampers loaded with $F_c = 94$ N.

evaluate the effect of the initial *static conditions* of the dampers on dynamic response of the blade, whereas the second set was performed to analyze the damper behavior at a very high excitation force with a very low static force F_c. In the first experimental activity, static condition means that the contact forces are only due to the static force F_c applied to the damper, without any dynamic excitation. It was observed that for a given F_c the static contact forces were not unique.

Different static condition for the same F_c were obtained with two distinct load sequences. In the first sequence, denoted as *loading*, dead weights were added monotonically up to the target value. In the second sequence, named *unloading*, the target value was exceeded first and then dead weights were removed to reach back the target value. Figures 12 and 13 show that the

static contact forces in the loading sequence are different from the unloading sequence even if F_c is the same. Figures 12 and 13 show the force measured by the load cells on the odd and even side respectively, whereas Figs. 14 and 15 show the contact forces computed according to the equations in Table 1. Moreover, the FRFs of the blade were measured for both the loading

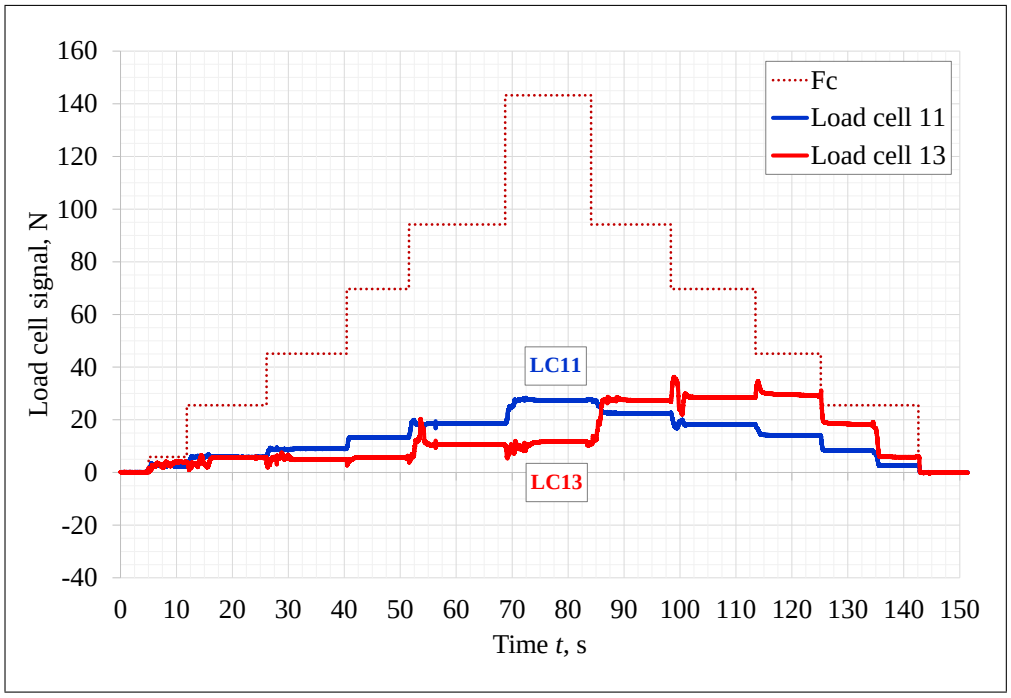

Figure 12: static forces measured by the load cells 11 and 13 (odd side) during the loading and unloading sequence.

and unloading conditions at the same damper static force F_c. The blade was excited with a stepped sine signal of amplitude 5N. Figure 11 presents the blade frequency response without and with dampers. The two different responses of the blade with dampers in Fig. 11 present the loading and unloading condition. By observing the response of the blade with dampers,

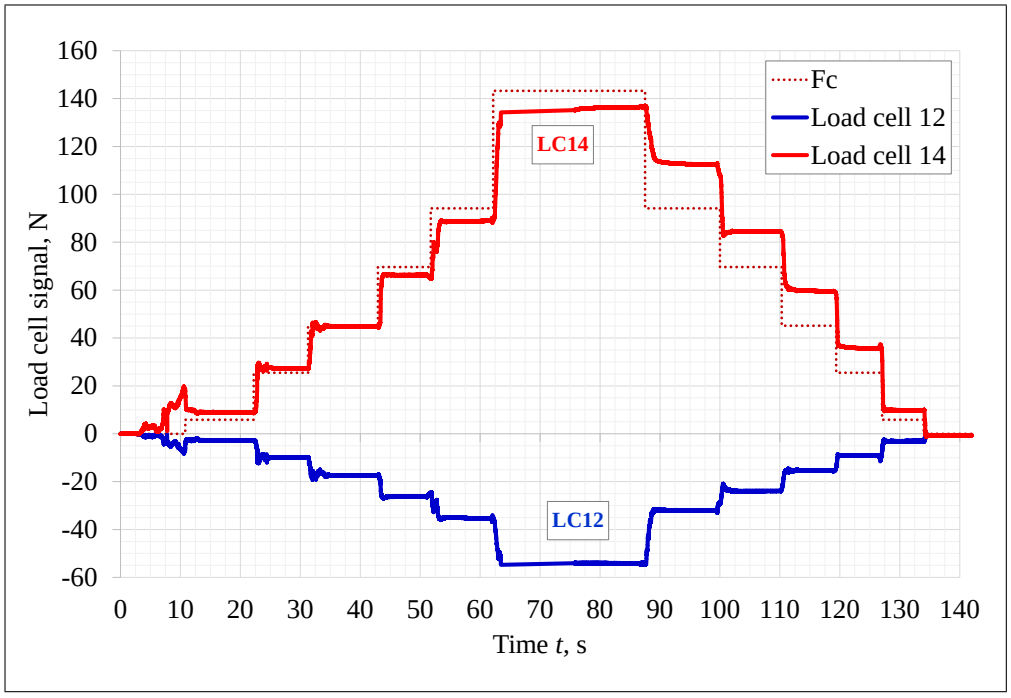

Figure 13: static forces measured by the load cells 12 and 14 (even side) during the loading and unloading sequence.

it is evident that the resonance frequency is higher in unloading than loading condition, whereas the response peak is lower in unloading condition. This behavior was observed by repeating the experiment several times. A similar trend was found by changing the value of F_c but detailed results are not reported here.

Modal parameters corresponding to loading and unloading were extracted by the response curves. The identification was performed with a best fit procedure assuming a single degree of freedom model with three parameters, namely the equivalent stiffness k_{eq}, the natural frequency ω_n and the damping ratio (viscous damping) ζ. Figure 16 shows the results of the best curve

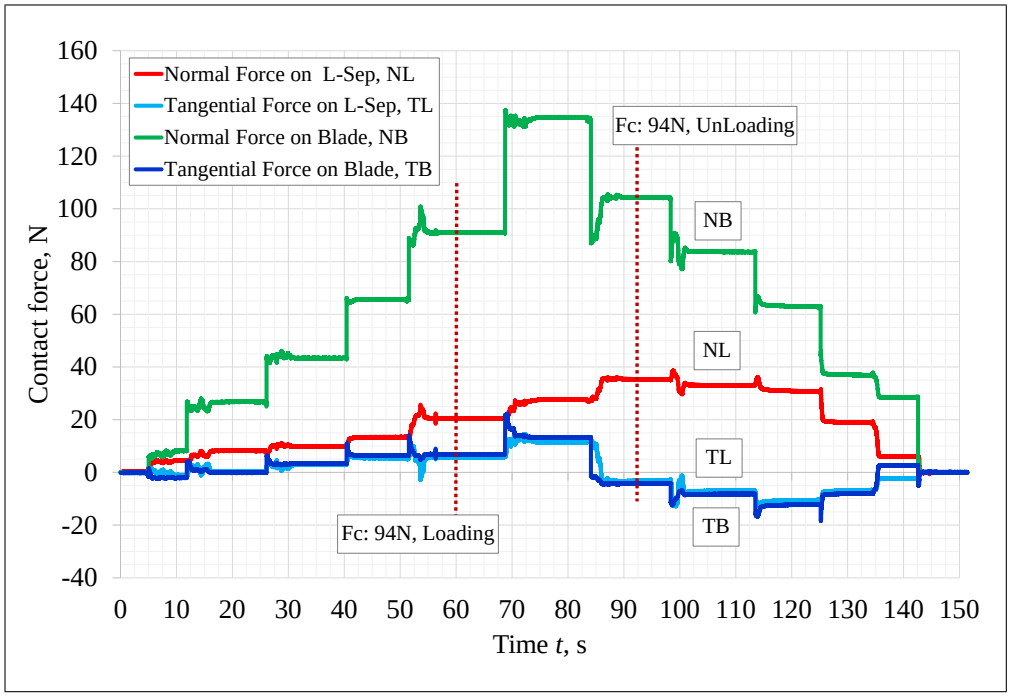

Figure 14: derived static contact forces on the L-Separator and on the blade during the loading and unloading sequence.

fitting and the value of the parameters. The analysis highlights that the damping ratio of the blade with dampers is not so different from the damping ratio of the blade without dampers at this higher F_c/F_e ratio. The relative displacement between the damper and blade is very small as shown in Fig. 17 and damper seems to be in stick condition. Observing the hysteresis loops in Fig. 17, it is evident that the damping introduced by the contact in these conditions is quite low, as it is proportional to the area enclosed by the loop. The main effect of the damper is to couple the blade with the support and increase the equivalent stiffness of the system. The reduction of the response peak is mainly due to increase in the stiffness of whole system by the added

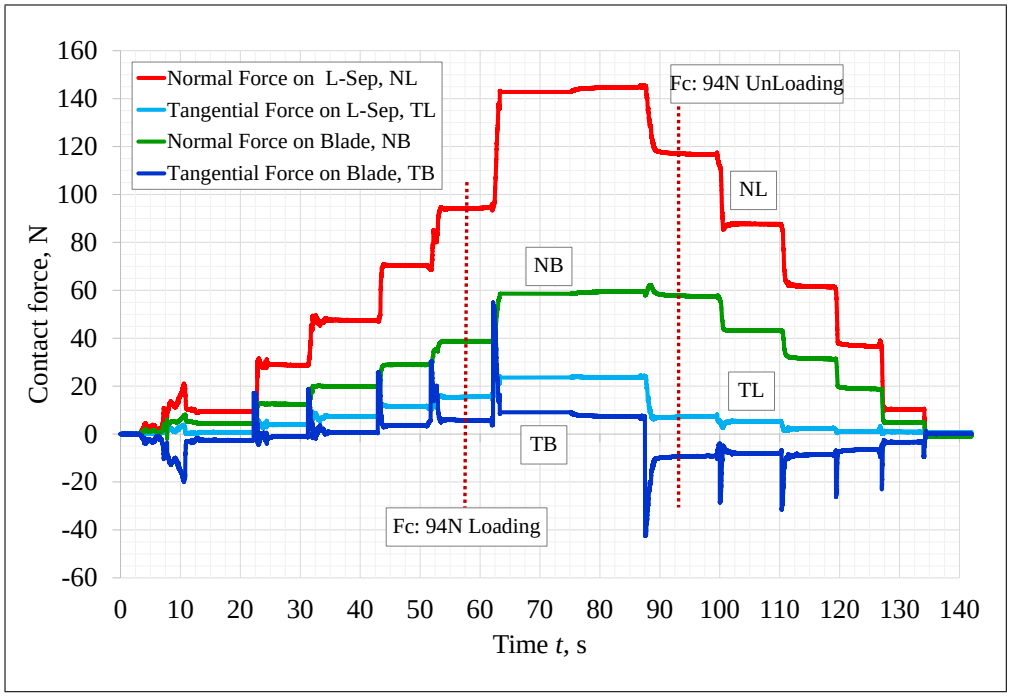

Figure 15: derived static contact forces on the L-Separator and on the blade during the loading and unloading sequence.

contact stiffness.

To better investigate the previously described behavior, the dynamics of the damper deserves a closer attention. In this regard, the damper kinematics was also measured in the second part of this experiment. The relative displacement δ between the damper and the blade was measured by using a differential laser vibrometer, see Fig.10. In this experiment, the blade was excited with a sinusoidal force, at the same amplitude of 5N as used during the FRF measurement, at a frequency close to the blade resonance. The measured relative displacement and tangential force give the well-known hysteresis loop. Figure 17, shows the hysteresis loops for both the loading

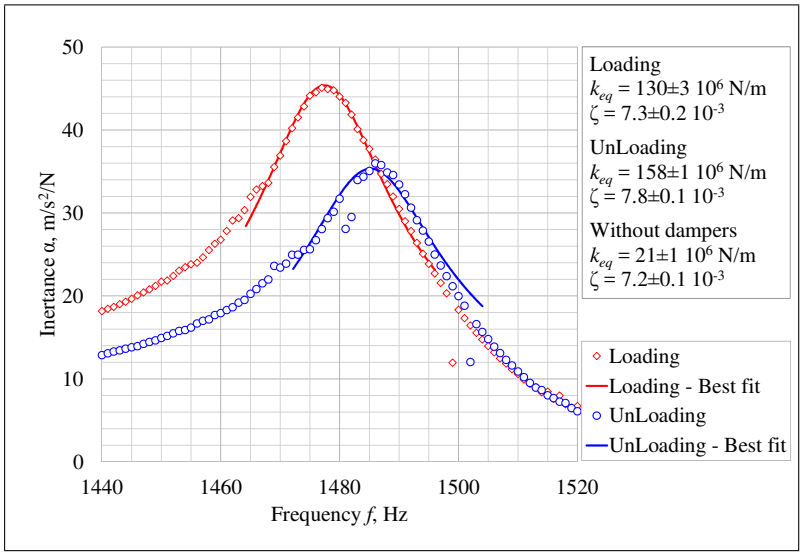

Figure 16: results of the best fit performed in Loading and UnLoading condition with static force on the damper $F_c = 94$ N. The objective function is a single degree of freedom model. Modal stiffness and damping are reported also for blade without dampers.

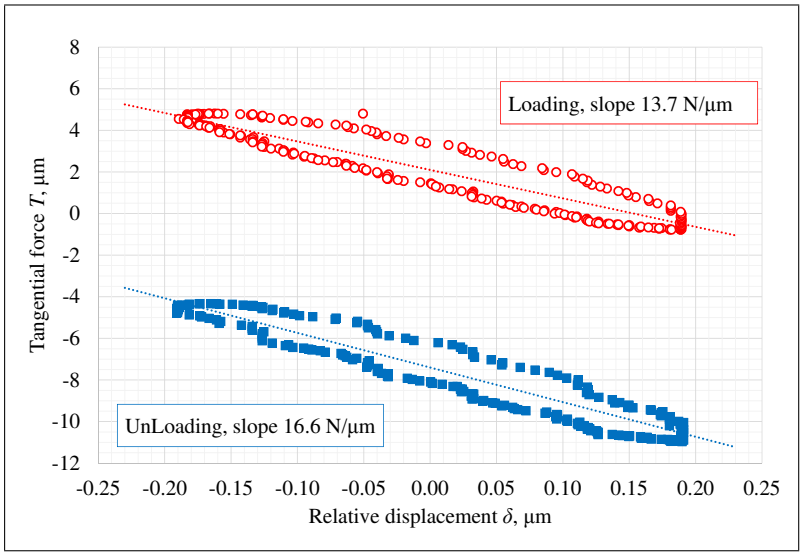

Figure 17: hysteresis loops measured in Loading and UnLoading conditions. The equivalent stiffness (slope) is reported for both conditions. The applied static load on the damper is $F_c = 94$ N.

and unloading conditions. The equivalent tangential contact stiffness k_T was determined by linearizing the tangential force. In a linear system the elastic forces F_{el} are in phase with the displacements, $F_{el} = k\,x$. Therefore, the equivalent tangential contact stiffness k_T was computed by projecting the tangential force on the relative displacement, $T\delta^T = k_T\,\delta\delta^T$, and averaging the projection over the period τ of the oscillation,

$$k_T = \frac{\frac{1}{\tau}\int_\tau T\delta\,dt}{\frac{1}{\tau}\int_\tau \delta^2\,dt}. \tag{4}$$

The contact stiffness at unloading sequence, $k_T = 16.6$ N/μm, was always found higher than the loading sequence, $k_T = 13.7$ N/μm. These results are consistent with the frequency shift observed during the response measurements in the first part of the experiment. In the second set of experiments

the blade was excited with a very high excitation force $F_e = 100$ N. This time the dampers were loaded with a small static force F_c= 25 N. The contact forces computed on the blade (even side) were compared with the respective contact forces computed on the L-Separator (odd side). A symmetric sector, from a dynamic point of view, is composed of the blade and one damper. Therefore, the contact forces on the even under-platform of the blade were expected to be equal to the contact forces on the odd L-Sep, with a phase shift of half period. Figures 18 and 19 show the contact force components on the L-Sep (Odd side) and on the blade (even side) respectively. The normal contact force components on the blade and on the L-Sep are compared in Fig. 20, while Fig. 21 compares the tangential contact force components. The forces have been shifted of half period to help the comparison. The force components on the blade and on the L-Sep show a good agreement and confirm the reliability of the measuring system. The small discrepancies are mainly due to the non-perfect symmetry of the contacts, the damper static force direction and the measurement uncertainty.

Moreover, lift off, namely the phenomenon in which the damper loses the contact with the platform, can be observed also. The portion encircled in Figs. 18 and 19 shows that the normal, and consequently the tangential, force decreases to zero. Value of the normal force less than zero is meaningless and is due to the measurement uncertainties. The lift off lasts for approximately 25% of a period.

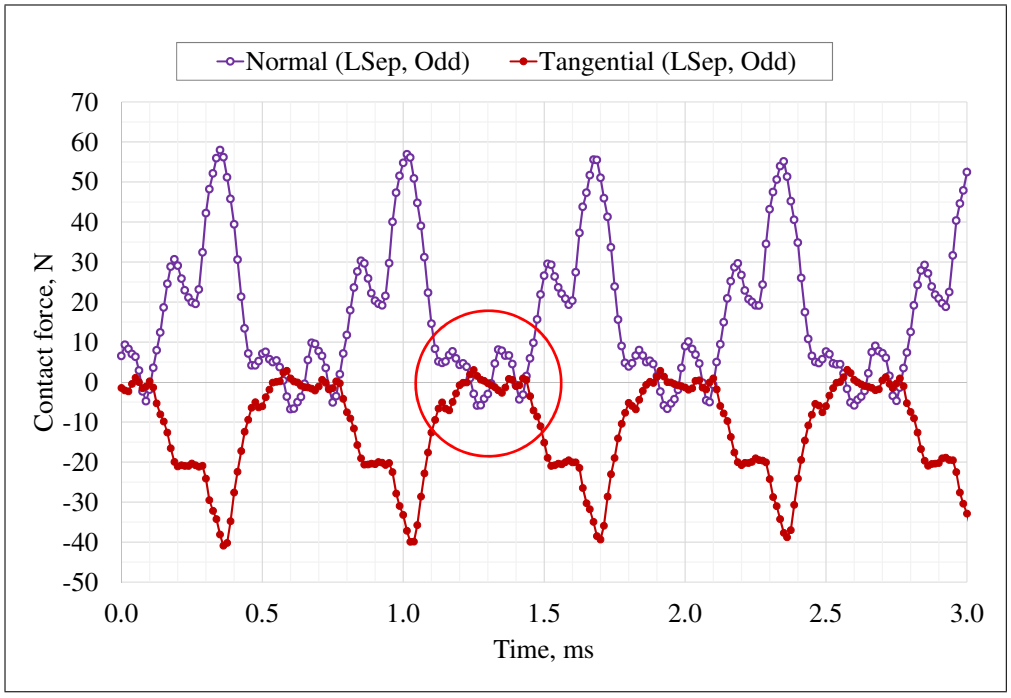

Figure 18: Contact forces on the L-Separator, odd side. Excitation force F_{ex}: 100 N, 1502 Hz. Static load on the damper 26 N.

7. Conclusion

The newly developed test rig presented in this paper is a reliable apparatus to explore the kinematics of under-platform dampers. A specific clamping mechanism loads the blade root with a pushing force that simulates the centrifugal force acting on the blade. This pushing force is controllable and measurable. This rig allows to test different blade/damper combinations with only minor changes in the setup of the rig. The force measuring system, whose main feature is the L-Separator, measures forces and relative displacement in the damper/blade contact. Most notably, this is the first rig to the author knowledge to measure contact forces of a system in which

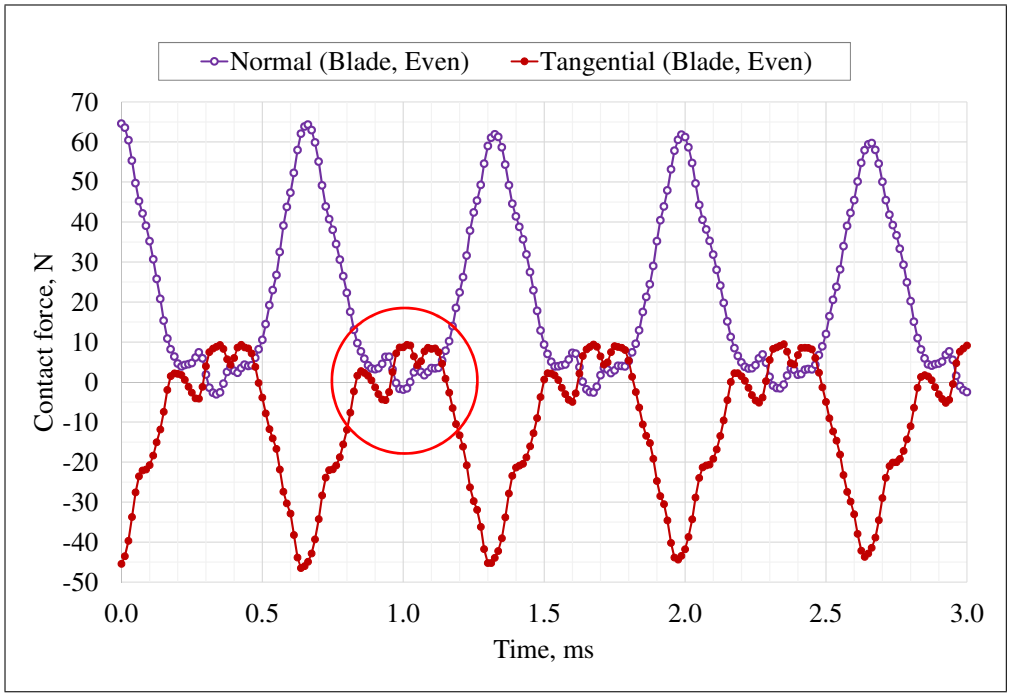

Figure 19: Contact forces on the Blade, even side. Excitation force F_{ex}: 100 N, 1502 Hz. Static load on the damper 26 N.

blade and dampers are dynamically coupled.

Reliability of measurements were assessed comparing the contact forces computed on one side of the blade with the respective contact forces computed on the L-Separator on the other side. The corresponding forces show the same trend, with a phase shift of half a period as expected. The small discrepancy are due to the non perfect symmetry of the contact.

The experimental results presented in this article emphasized how the static conditions of the damper affects the blade response. Prior works [29, 30] have discussed the effect of the damper static conditions on the blade dynamics. In the presented work different static conditions were investigated by

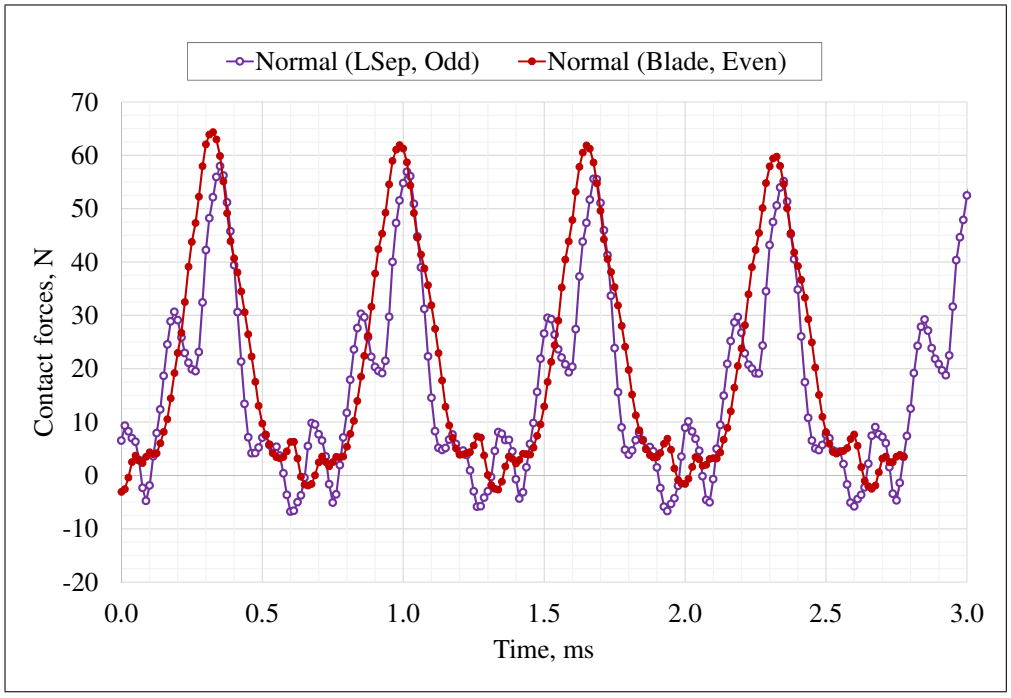

Figure 20: comparison of normal contact force on the L-Separator (odd side) and the blade (even side).Excitation force F_{ex}: 100 N, 1502 Hz. Static load on the damper 26 N.

applying the same static load, simulating the centrifugal force, to the damper with the purposely defined Loading/UnLoading sequence. The resonance frequency of the blade was found always higher and the amplitude peak lower during UnLoading with respect to the Loading, provided the static load on the damper is the same. The modal parameters were identified with a best fitting on the blade frequency response. The modal stiffness was found always higher in UnLoading than in Loading condition. A deeper analysis of the contact was performed to evaluate, through the hysteresis loops, the contact stiffness. Also the contact stiffness was found always higher in unloading than in loading condition. This observation is in step with the dynamic

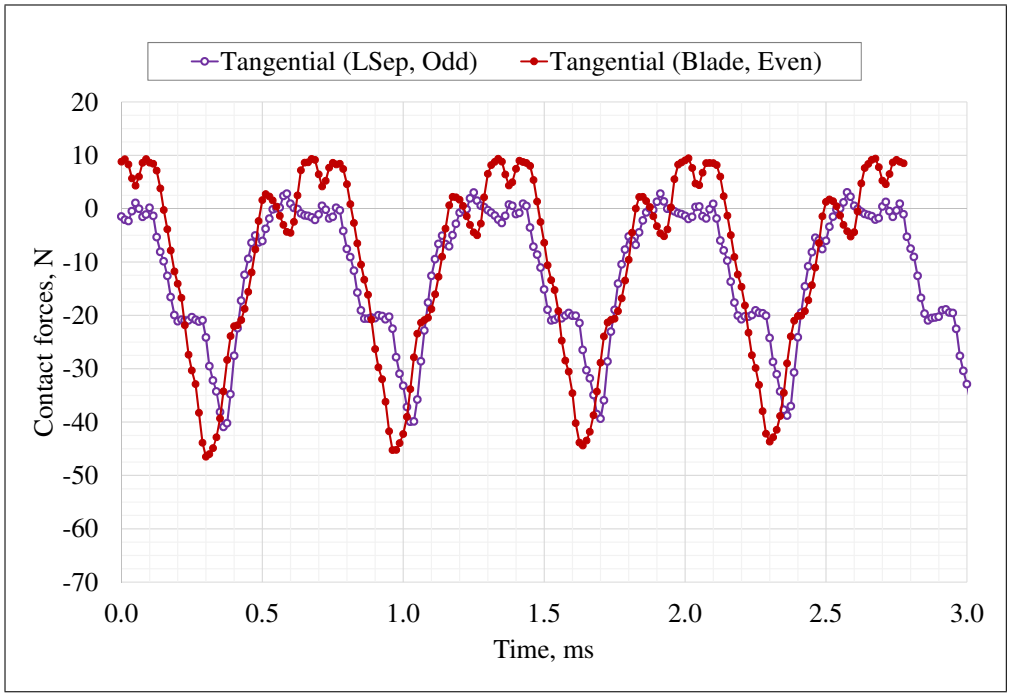

Figure 21: comparison of tangential contact force on the L-Separator (odd side) and the blade (even side).Excitation force F_{ex}: 100 N, 1502 Hz. Static load on the damper 26 N.

behavior of the blade and backs up the modal stiffness calculation. Different static conditions affect both the frequency shift and the resonance peak amplitude. For the blade under investigation the frequency shift was found negligible, less than 1% in average, whereas the change in peak amplitude is significant, around 25%.

This outcome explains the scattering of the response functions measured on blade/damper systems even if the same nominal static load is applied to the damper.

References

[1] R. D. Mindlin, Compliance of elastic bodies in contact, J. Appl. Mech. 16 (1949) 259–268. doi:10.1007/978-1-4613-8865-4_24.

[2] J. H. Griffin, Friction damping of resonant stresses in gas turbine engine airfoils, J. Eng. Power-Trans. ASME 102 (2) (1980) 329–333. doi:10.1115/1.3230256.

[3] C. H. Menq, J. H. Griffin, J. Bielak, The influence of microslip on vibratory response, part ii: A comparison with experimental results, J. Sound Vibr. 107 (2) (1985) 295–307. doi:10.1016/0022-460X(86)90239-7.

[4] W. Sextro, K. Popp, I. Wolter, Improved reliability of bladed disks due to friction dampers, in: ASME Turbo Expo: Power for Land, Sea, and Air, Vol. 4: Manufacturing Materials and Metallurgy; Ceramics; Structures and Dynamics; Controls, Diagnostics and Instrumentation; Education, Orlando, Florida, USA, 1997, p. V004T14A035. doi:10.1115/97-GT-189.

[5] K. Y. Sanliturk, D. J. Ewins, A. B. Stanbridge, Underplatform dampers for turbine blades: Theoretical modeling, analysis, and comparison with experimental data, in: ASME Turbo Expo: Power for Land, Sea, and Air, Vol. 4: Manufacturing Materials and Metallurgy; Ceramics; Structures and Dynamics; Controls, Diagnostics and Instrumentation; Education, 1999, p. V004T03A037. doi:10.1115/99-GT-335.

[6] L. Panning, W. Sextro, K. Popp, Optimization of interblade friction damper design, in: ASME Turbo Expo: Power for Land, Sea, and Air,

Vol. 4: Manufacturing Materials and Metallurgy; Ceramics; Structures and Dynamics; Controls, Diagnostics and Instrumentation; Education, Munich, Germany, 2000, p. V004T03A068. doi:10.1115/2000-gt-0541.

[7] J. Szwedowicz, M. Kissel, B. Ravindra, K. R., Estimation of contact stiffness and its role in the design of a friction damper, in: ASME Turbo Expo: Power for Land, Sea, and Air, Vol. 4: Manufacturing Materials and Metallurgy; Ceramics; Structures and Dynamics; Controls, Diagnostics and Instrumentation; Education, New Orleans, Louisiana, USA, 2001, p. V004T03A049. doi:10.1115/2001-GT-0290.

[8] A. Bessone, F. Toso, T. Berruti, Investigation on the dynamic response of blades with asymmetric under platform dampers, in: ASME Turbo Expo: Power for Land, Sea, and Air, Vol. 7B: Structures and Dynamics, Montreal, Quebec, Canada, 2015, p. V07BT33A003. doi:10.1115/GT2015-42597.

[9] C. Firrone, Measurement of the kinematics of two underplatform dampers with different geometry and comparison with numerical simulation, J. Sound Vibr. 323 (2009) 313–333.

[10] L. Pesaresi, L. Salles, A. Jones, J. Green, C. Schwingshackl, Modelling the nonlinear behaviour of an underplatform damper test rig for turbine applications, Mech. Syst. Signal Proc. 85 (2017) 662–679. doi:10.1016/j.ymssp.2016.09.007.

[11] B. D. Yang, C. H. Menq, Characterization of contact kinematics and

application to the design of wedge dampers in turbomachinery blading: Part 2 – prediction of forced response and experimental verification., J. Eng. Gas. Turbines Power-Trans. ASME 120 (2) (1998) 418–423. doi:10.1115/1.2818139.

[12] E. Cigeroglu, N. An, C. H. Menq, Forced response prediction of constrained and unconstrained structures coupled through frictional contacts, J. Eng. Gas. Turbines Power-Trans. ASME 131 (2) (2009) 022505–022505–11. doi:10.1115/1.2940356.

[13] T. Berruti, A test rig for the investigation of the dynamic response of a bladed disk with underplatform dampers, Mech. Res. Commun. 37 (6) (2010) 581–583. doi:10.1016/j.mechrescom.2010.07.008.

[14] J. Szwedowicz, C. Gibert, T. P. Sommer, R. Kellerer, Numerical and experimental damping assessment of a thin-walled friction damper in the rotating setup with high pressure turbine blades, J. Eng. Gas. Turbines Power-Trans. ASME 130 (1) (2008) 012502–012502–10. doi:10.1115/1.2771240.

[15] I. A. Sever, E. P. Petrov, D. J. Ewins, Experimental and numerical investigation of rotating bladed disk forced response using underplatform friction dampers, J. Eng. Gas. Turbines Power-Trans. ASME 130 (4) (2008) 042503–11. doi:10.1115/1.2903845.

[16] S. Zucca, D. Di Maio, D. J. Ewins, Measuring the performance of underplatform dampers for turbine blades by rotating laser doppler vibro-

meter, Mech. Syst. Signal Proc. 32 (2012) 269–281. doi:10.1016/j.ymssp.2012.05.011.

[17] K. Y. Sanliturk, A. B. Stanbridge, D. J. Ewins, Friction dampers: measurement, modelling and application to blade vibration control, in: Proceedings of Design Engineering Technical Conferences, Vol. 84, 1995, pp. 1377–1382.

[18] S. Filippi, A. Akay, M. M. Gola, Measurements of tangential contact hysteresis during microslip, J. Tribol. 126 (2004) 482–489.

[19] C. Schwingshackl, E. Petrov, D. Ewins, Validation of test rig measurements and prediction tools for friction interface modelling, in: ASME Turbo Expo: Power for Land, Sea, and Air, Vol. 6, 2010. doi:10.1115/GT2010-23274.

[20] M. Lavella, D. Botto, M. M. Gola, Test rig for wear and contact parameters extraction for flat-on-flat contact surfaces, in: ASME/STLE International Joint Tribology Conference, 2011, pp. 307–309. doi:10.1115/IJTC2011-61234.

[21] D. Botto, M. Lavella, M. M. Gola, Measurement of contact parameters of flat on flat contact surfaces at high temperature, in: Turbo Expo: Power for Land, Sea, and Air, Vol. 7: Structures and Dynamics, Parts A and B, 2012, pp. 1325–1332. doi:10.1115/GT2012-69677.

[22] C. W. Schwingshackl, E. P. Petrov, D. J. Ewins, Measured and estimated friction interface parameters in a nonlinear dynamic analysis, Mech.

Syst. Signal Proc. 28 (2012) 574–584. doi:10.1016/j.ymssp.2011.10.005.

[23] M. Lavella, D. Botto, M. M. Gola, Design of a high-precision, flat-on-flat fretting test apparatus with high temperature capability, Wear 302 (2013) 1073–1081.

[24] M. M. Gola, M. Braga dos Santos, T. Liu, Design of a new test rig to evaluate under-platform damper performance, in: ASME 10th Biennial Conference on Engineering Systems Design and Analysis, Vol. 5, 2010, pp. 85–95. doi:10.1115/ESDA2010-24268.

[25] M. M. Gola, M. Bragas dos Santos, T. Liu, Measurement of the scatter of underplatform damper hysteresis cycle: experimental approach, in: ASME International Design Engineering Technical Conferences and Computers and Information in Engineering Conference, Vol. 1: 24th Conference on Mechanical Vibration and Noise, Parts A and B, 2012, pp. 359–369. doi:10.1115/detc2012-70269.

[26] M. M. Gola, C. Gastaldi, Understanding complexities in underplatform damper mechanics, in: ASME Turbo Expo: Power for Land, Sea, and Air, Vol. 7A: Structures and Dynamics, 2014, p. V07AT34A002. doi:10.1115/GT2014-25240.

[27] M. M. Gola, T. Liu, A direct experimental-numerical method for investigations of a laboratory under-platform damper behavior, Int. J. Solids Struct. 51 (25-26) (2014) 4245–4259.

[28] C. Gastaldi, M. M. Gola, Pre-optimization of asymmetrical underplatform dampers, J. Eng. Gas. Turbines Power-Trans. ASME 16 (2016) 1229.

[29] S. Zucca, D. Botto, M. Gola, Range of variability in the dynamics of semi-cylindrical friction dampers for turbine blades, in: ASME Turbo Expo: Power for Land, Sea, and Air, Vol. 5: Structures and Dynamics, Parts A and B, 2008, pp. 519 –529. doi:10.1115/GT2008-51058.

[30] C. M. Firrone, S. Zucca, M. Gola, The effect of underplatform dampers on the forced response of bladed disks by a coupled static/dynamic harmonic balance method, Int. J. Non-Linear Mech. 46 (2) (2011) 363–375. doi:10.1016/j.ijnonlinmec.2010.10.001.

[31] NTN, NTN Needle Roller Bearing handbook, Cat. No. 9013/A, NTN.BEARING CORPORATION, 2009, Ch. Needle Roller Bearing, p. 8.

[32] K. L. Johnson, Contact mechanics, Cambridge University Press, Cambridge, 1985. doi:10.1017/cbo9781139171731.